HarmonicNeRF: Geometry-Informed Synthetic View Augmentation for 3D Scene Reconstruction in Driving Scenarios

Anonymous Authors

ABSTRACT

In the realm of autonomous driving, achieving precise 3D reconstruction of the driving environment is critical for ensuring safety and effective navigation. Neural Radiance Fields (NeRF) have shown promise in creating highly detailed and accurate models of complex environments. However, the application of NeRF in autonomous driving scenarios encounters several challenges, primarily due to the sparsity of viewpoints inherent in camera trajectories and the constraints on data collection in unbounded outdoor scenes, which typically occur along predetermined paths. This limitation not only reduces the available scene information but also poses significant challenges for NeRF training, as the sparse and path-distributed observational data lead to under-representation of the scene's geometry. In this paper, we introduce HarmonicNeRF, a novel approach for outdoor self-supervised monocular scene reconstruction. HarmonicNeRF capitalizes on the strengths of NeRF and enhances surface reconstruction accuracy by augmenting the input space with geometry-informed synthetic views. This is achieved through the application of spherical harmonics to generate novel radiance values, taking into careful consideration the color observations from the limited available real-world views. Additionally, our method incorporates proxy geometry to effectively manage occlusion, generating radiance pseudo-labels that circumvent the limitations of traditional image-warping techniques, which often fail in sparse data conditions typical of autonomous driving environments. Extensive experiments conducted on the KITTI, Argoverse, and NuScenes datasets demonstrate our approach establishes new benchmarks in synthesizing novel depth views and reconstructing scenes, significantly outperforming existing methods.

CCS CONCEPTS

• **Computing methodologies** → **Computer vision**; **Computer graphics**.

KEYWORDS

Neural Radiance Fields, Sparse Views, Ray Augmentation, Autonomous Driving

1 INTRODUCTION

In recent years, with the rapid advancement of autonomous driving technology, 3D reconstruction has become a crucial component for ensuring precision in navigation and overall safety. Amidst this technological evolution, Neural Radiance Fields (NeRF) [28] have emerged as a groundbreaking 3D reconstruction technique, gaining widespread attention for their ability to generate highly detailed and accurate models of complex environments. Unlike traditional Multi-View Stereo (MVS) [7, 12, 50] methods, NeRF utilizes deep learning to model environments, capable of synthesizing continuous and photorealistic images, thereby significantly enhancing reconstruction quality and visual fidelity. Furthermore, NeRF's capability to synthesize intricate autonomous driving scenes [16, 21] enriches training datasets for autonomous systems, aiding in the improvement of their generalizability and decision-making quality.

Despite the remarkable performance of NeRF and its derivatives in targeted synthetic rendering datasets, their scene reconstruction performance significantly diminishes when applied to specific autonomous driving datasets such as KITTI [14] and NuScenes [4]. This decline is primarily attributed to the limited viewpoints provided by autonomous driving scenarios, failing to offer sufficient perspective information for high-quality synthesis. Additionally, the camera trajectories in autonomous driving are characterized by sparse viewpoints of single self-motion, differing from the object-centered forms previously encountered. The presence of moving objects in autonomous driving scenes introduces variations in lighting and geometry over time, resulting in artifacts in synthesized images and a decrease in reconstruction effectiveness. The original NeRF model does not account for moving objects, limiting its application in autonomous driving contexts.

To address the limitations of NeRF in modeling dynamic scenes undergoing motion, several scholars have proposed extensions to the NeRF network architecture. Innovations such as D-NeRF [35] and NRNeRF [41] for scenes with non-rigid deformations, and time-variable dynamic radiance fields like NSFF [22] , NeRFlow [10], DynamicNeRF [13], and RoDynRF [23] have been introduced. These adaptations incorporate temporal dimensions or consider non-rigid transformations to accommodate scene dynamics. Moreover, concerns regarding the original NeRF model's size and its direct application to autonomous driving scenarios leading to significant artifacts and reduced visual fidelity have led to the development of solutions like Mip-NeRF [1], which considers positions as conical sections of a light ray rather than points to mitigate aliasing effects on NeRF performance. NeRF in the Wild [25] addresses varying environmental conditions by encoding appearances.

Although these methods have somewhat enhanced NeRF's capability in dynamic scene reconstruction, they generally fail to fully address the challenges posed by the sparse viewpoints and path-distributed data collection inherent in autonomous driving scenes. In response to these issues, this paper introduces a novel geometry-guided ray augmentation technique specifically designed for sparse view scene reconstruction in driving scenarios. Our approach not only effectively manages challenges presented by dynamic objects

Unpublished working draft. Not for distribution.

Permission to make digital or hard copies of all or part of this work for personal or classroom use is granted without fee provided that copies are not made or distributed for profit or commercial advantage and that copies bear this notice and the full citation on the first page. Copyrights for components of this work owned by others than the author(s) must be honored. Abstracting with credit is permitted. To copy otherwise, or republish, to post on servers or to redistribute to lists, requires prior specific permission and/or a fee. Request permissions from permissions@acm.org.
ACM MM, 2024, Melbourne, Australia
© 2024 Copyright held by the owner/author(s). Publication rights licensed to ACM.
ACM ISBN 978-x-xxxx-xxxx-x/YY/MM
https://doi.org/10.1145/nnnnnnn.nnnnnnn

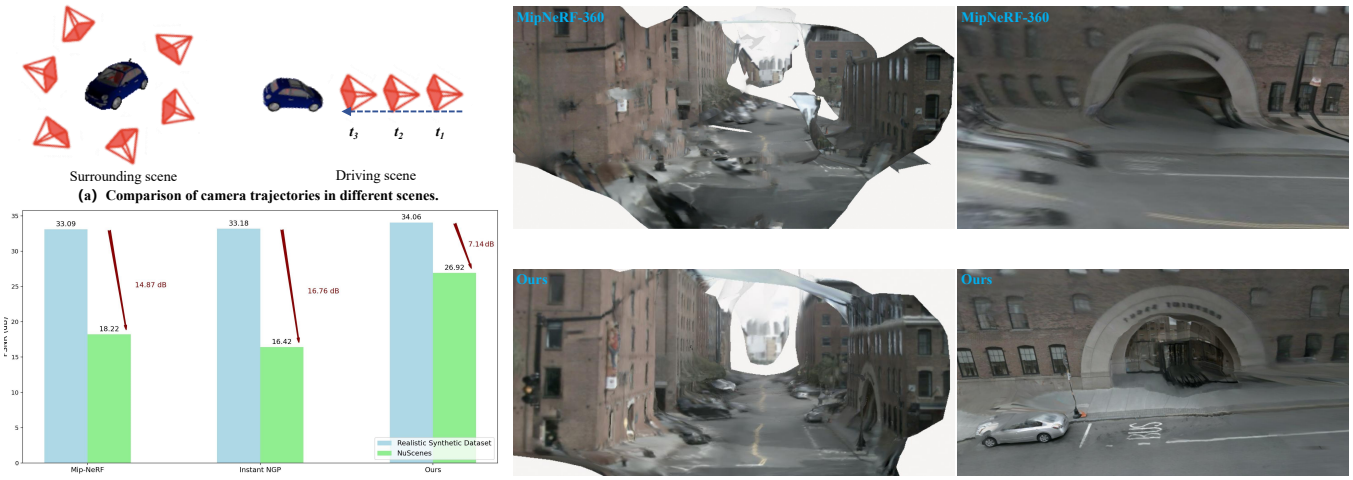

(a) Comparison of camera trajectories in different scenes.

(b) Comparison of reconstruction metrics across different scenes.

(c) Comparison of 3D reconstruction visualization in different scenes.

Figure 1: (a)illustrates the differing camera paths in both general surrounding scenes and specific driving scenarios. The camera trajectories in driving scenes are depicted as more linear and path-constrained, indicative of the typical movement patterns in autonomous driving data collection, as opposed to the more varied viewpoints found in general scenes. (b) shows our method's effectiveness in dealing with the challenges of sparse and dynamic driving environments. Our reconstruction in (c) demonstrates significantly clearer and more accurate geometries

and sparse viewpoints but also significantly improves scene reconstruction accuracy from sparse views through the innovative application of proxy geometry and spherical harmonics. Experiments conducted on challenging autonomous driving datasets such as KITTI, Argoverse [5], and NuScenes validate the superiority of our method, establishing new benchmarks in 3D scene reconstruction for the domain of autonomous driving.

In summary, our contributions are as follows:

- We leverage spherical harmonics to comprehensively integrate all color observations at a 3D point. This approach enables the generation of pseudo-labels that align with the natural distribution of radiance, enhancing the consistency and accuracy of scene illumination and texture.
- We introduce a novel use of proxy geometry to address occlusion challenges during the ray augmentation process. This strategy ensures that point radiance is unconfounded, facilitating the reconstruction of more accurate surfaces from sparse viewpoints, a common scenario in autonomous driving environments.
- Our method is designed as a versatile, plug-and-play solution, compatible with existing sparse implicit neural surface reconstruction techniques. It demonstrates exceptional performance in sparse view reconstruction tasks, achieving superior results in driving scenarios without requiring additional data or extensive pre-training.

2 RELATED WORK

Neural Surface Reconstruction Recently, neural implicit representations have demonstrated superior effectiveness in various tasks such as 3D object [8, 26, 34] and scene representation [28, 37, 38], novel view synthesis [2, 28, 45] and multi-view 3D reconstruction [31, 32, 46, 52]. Among them, NeRF and its variants [2, 28] demonstrated state-of-the-art performance for novel view synthesis with differentiable volumetric rendering. However, they require dense images for input and it is hard to extract high-quality geometry because the predicted density field lacks sufficient constraints. Other works utilizing surface rendering [31] produce more accurate modeling but require additional constraints such as ground truth masks or depth priors for supervision [52, 54]. Several later studies combine the advantages of surface and volume representation, generating satisfying surfaces with only image inputs [32, 46, 51]. For example, NeuS [46] combined volume rendering with signed distance functions to circumvent the problem of insufficient surface constraint in the original NeRF. The sampling efficiency was further improved to allow for reconstructing in the wild scenes [39]. UNISURF [32] also unifies surface and volume rendering but with occupancy fields. Similar to them, our work also only requires multi-view images for 3D reconstruction.

Large-Scale Scene Reconstruction NeRF's static assumptions falter in the dynamic, expansive scenes of autonomous driving, where direct application incurs artifacts and fidelity loss due to lighting and occlusion changes. Tackling NeRF's capacity limitations, methods like Mega-NeRF [43] and Block-NeRF [40] divide scenes into smaller, manageable NeRF segments, improving training efficiency and computational feasibility. Mip-NeRF [1] addresses aliasing by representing positions as conical sections rather than points, enhancing rendering quality. Approaches like Block-NeRF's adaptation of NeRF in the Wild [25] encode varying appearances for realistic lighting condition reconstructions. Recent extensions such

as LocalRF [27], READ [21], and S-NeRF [48] further NeRF's applicability in autonomous driving, dealing with changing geometries and appearances characteristic of these environments.

Implicit Representation with Sparse Views In the realm of autonomous driving, reconstructing environments from sparse views is a pressing challenge due to the sporadic nature of data acquisition on the road. Two primary strategies have emerged to adapt NeRF for sparse input: leveraging pre-trained CNNs to extract image features from multi-view inputs or using sparse point clouds from Structure-from-Motion (SfM) for additional supervision.

PixelNeRF [53] innovatively simulates continuous neural scenes from a few input images, employing pre-trained layers of convolutional neural networks (CNNs) and bilinear interpolation. This method enhances the feature extraction process for each sampling point, fully utilizing the characteristics of input images. It then conveys the extracted feature points, spatial locations, and viewing directions to the NeRF network, enabling the construction of continuous static scenes from sparse image sets [53]. The General Radiance Field (GRF) [42] adopts a similar approach to PixelNeRF but differs in that it operates in a standardized canonical space, offering more generality and versatility, particularly under the varying conditions encountered in autonomous driving scenarios. Point-NeRF [49] combines the explicit representation of point clouds with the implicit NeRF technique. It harnesses the strengths of both 3D representation forms and adapts efficiently to the surfaces of scenes, a crucial feature for capturing the complexities of driving environments [6].

Other methods such as GeoNeRF [18] and DietNeRF [17] propose novel supervision techniques that enrich the input data for NeRF with semantic consistency or spatial geometry from unobserved viewpoints. These methods mitigate issues like floating artifacts that are common when dealing with sparse views but often require additional datasets for training, which may introduce domain generalization challenges. HarmonicNeRF bypasses the need for pre-training entirely, diverging from the aforementioned works. Instead of regularization or relying on scene priors, we focus on fitting the radiance distribution for each surface point, using it as augmented information. We posit that the radiance distribution at a point is a harmonic function, decomposable into a spherical harmonic expansion. This insight leads us to develop a physically grounded pipeline to generate precise pseudo labels for radiance supervision, tailor-made for the dynamic and variable conditions present in autonomous driving data collection [9, 20].

3 PRELIMINARIES: NEUS

NeuS [46] represents a 3D scene as two continuous functions both parametrized by a multi-layer perception (MLP). The first one is a signed-distance function that takes as input 3D position $\mathbf{x} = (x, y, z)$ and predicts its signed distance: $f_1(\mathbf{x}) \rightarrow s$, and the other takes both $\mathbf{x}$ and its viewing direction $\mathbf{d}$ and predicts its view-dependent color: $f_2(\mathbf{x}, \mathbf{d}) \rightarrow \mathbf{c}$.

Similar to NeRF [28], the color of a pixel in NeuS [46] only depends on the radiance along a ray with no other lighting factors. For a camera ray $\mathbf{r}(t) = \mathbf{o} + t\mathbf{d}$ with center $\mathbf{o}$ and direction $\mathbf{d}$, its color can be derived with volume rendering [19]. In practice, NeuS samples N points along $\mathbf{r}(t)$ with $t = t_1, ...t_N, t_i < t_{i+1}$ and approximate the per-pixel color with the following:

$$\hat{\mathbf{C}}(\mathbf{r}) = \sum_{i=1}^{N} T_i \alpha_i \mathbf{c}_i, \tag{1}$$

$$T_i = \prod_{j=1}^{i-1} (1 - \alpha_j), \tag{2}$$

where α_i is the discrete opacity value that is a function of the probability density function of f_1, and T_i is the accumulated transmittance which indicates the probability that a ray traverses from t_1 to t_i without hitting any particle. NeuS exploits volume rendering to minimize the mean-squared error (MSE) between the predicted ray color $\hat{\mathbf{C}}(\mathbf{r})$ and the ground truth $\mathbf{C}(\mathbf{r})$:

$$\mathcal{L}_{\text{MSE}} = \sum_{\mathbf{r}} \|\hat{\mathbf{C}}(\mathbf{r}) - \mathbf{C}(\mathbf{r})\|_2^2. \tag{3}$$

Besides color loss, it also leverages an L1 regularization and a mask loss if available. With successful minimization, the formulation of NeuS enables the network to learn a signed-distance function that represents an accurately reconstructed surface.

4 METHODS

When limited images and corresponding training rays are given, from Section 3, only a small proportion of the 3D space has supervision, while the results of the rest space purely rely on the interpolation ability of the network. Therefore, the main goal of our paper is to augment the supervision signal of Implicit Neural Representation (INR) by inferring rays from unseen viewpoints based on limited inputs and the reconstructed INR in an accurate way. Particularly, we found that model the problem of inferring unseen radiance as fitting the radiance maps for spatial points, and the radiance map of each point could be estimated from the known radiance of that point based on our prior radiance map function.

In this work, we introduce HarmonicNeRF: Enhancing Neural Radiance Fields with Visibility-Driven Spherical Harmonics, a novel approach that significantly advances the capabilities of neural radiance fields by incorporating spherical harmonics for accurate radiance map estimation and employing visibility checks alongside surface ray casting for improved scene reconstruction from sparse viewpoints.

In the following of this section, we introduce the details of our method. Our radiance augmentation algorithm is composed of three steps: Surface Ray Casting in Section 4.1, Visibility Checking in Section 4.2, and Radiance Map Estimation in Section 4.3.

4.1 Surface Ray Casting

Same to NeRF, the input to our method is a set of posed images $\{I_i\}_{i=1}^{N}$, where N is the number of images. The original training set is denoted by $\mathcal{R} = \{(\mathbf{r}, \mathbf{c})\}$, in which $\mathbf{r}$ and $\mathbf{c}$ are the ray directions and ray color. Since our method relies on the rough scene geometry, we first train a radiance field for a few thousand steps and construct the mesh with marching cubes [24]. The vertices of this rough mesh are regarded as points lying on the surface. Then starting from these surface points $\mathbf{v}$, we shoot a number of rays $\mathbf{r}_{rand} \in \mathcal{R}$ in random directions. We denote the ray casted as $\tilde{\mathcal{R}}_{\mathbf{v}}$. We ensure that the angle between new rays and the surface normal of $\mathbf{v}$ is less than $\frac{\pi}{2}$, so these candidates for augmented rays are confident.

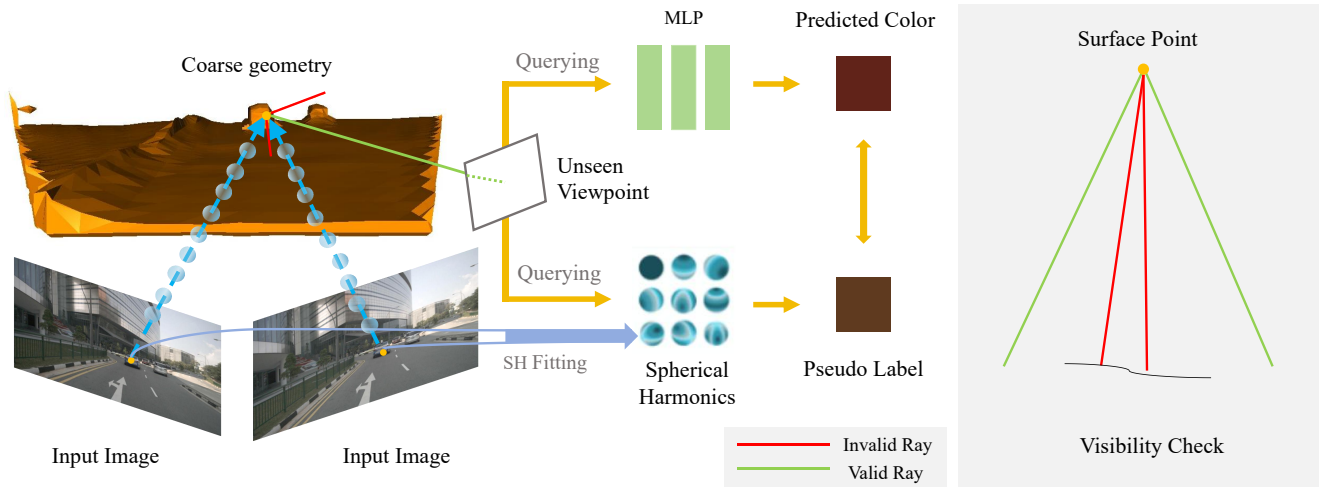

Figure 2: Method Overview. We exploit the coarse geometry in radiance field training to guide its augmentation with sparse inputs. (left) For a surface point v, we aggregate the color observations from all inputs to fit a spherical harmonics expansion, thus the pseudo labels for all the augmented rays passing through v can be obtained through querying the SH, (right) when generating augmented rays, we check their visibility and exclude those cannot be actually observed.

4.2 Visibility Check

However, some rays in $\tilde{\mathcal{R}}_{\mathbf{v}}$ might not actually be observed from a valid viewport since they will hit the mesh and get occluded. Figure 2 shows an example of this case. To filter out those invalid rays, we include an additional visibility check step to exclude those invalid rays. Specifically, for each ray $\mathbf{r}_{aug}$, we march from the starting point $\mathbf{v}$ according to the scene signed-distance field (SDF) and terminate when the surface is reached or achieve the maximum number of steps. Since the ray marching method is efficient, we integrate it directly into the training pipeline without any offline computation.

Algorithm 1 Ray Marching for Visibility Check

Input: pos (starting point), sdf (signed-distance function)
Output: visible or not

```
step := 0
d := sdf(pos)
while d > ϵ and step < max_steps do
    pos = pos + dir * d
    d = sdf(pos)
    step = step + 1
end while
if step < max_steps then
    return true  // visible
else
    return false  // invisible
end if
```

4.3 Radiance Map

After the visibility check, rays in $\tilde{\mathcal{R}}_{\mathbf{v}}$ are ensured to be observed from at least one camera viewpoint. The next question is what's the proper radiance value of rays in $\tilde{\mathcal{R}}_{\mathbf{v}}$? In previous ray augmentation methods [55], a surface ray has only one known radiance value, since the source view visibility check is not performed, thus they simply assign a color from one input view, which neglects the view-dependent effect and leads to inconsistent pseudo label. However, as shown in the previous discussion, a point in the scene surface could be seen from multiple views and we actually have more information regarding the radiance of surface point $\mathbf{v}$. Thus, a main contribution of our method illustrated as follows is that we utilize all reasonably credible information to reconstruct the radiance distribution of surface point $\mathbf{v}$ to infer the radiance of novel rays. Actually, not only did we fit the radiance distribution but also we achieved extrapolation using spherical harmonics expansion fitting.

Our method handles the inference of radiance in two situations. Firstly in the simpler case, if the point can only be seen from less than N_v views (N_v is empirically 10 in our experiment), we think that we don't have enough information to reconstruct the radiance distribution. Thus, the radiance value of a randomly chosen view is assigned to all new rays origin from point $\mathbf{v}$. This is basically in accordance with the previous method.

If the point $\mathbf{v}$ under processing can be viewed from more than N_v views, then in this case we try to infer a distribution of radiance over all viewing directions. Our solution to this problem is to fit a spherical harmonic expansion, which is widely used in precompute radiance transfer and environment maps in computer graphics. We represent the radiance distribution using spherical harmonics:

$$\mathbf{c}_{\mathbf{v}}(\mathbf{d}) = \sum_{\ell=0}^{\ell_{\max}} \sum_{m=-\ell}^{\ell} k_\ell^m Y_\ell^m(\mathbf{d}), \tag{4}$$

where $\mathbf{c}_{\mathbf{v}}(\mathbf{d})$ is the radiance of point $\mathbf{v}$ viewing from $\mathbf{d}$. Namely, for vertice $\mathbf{v}$, we back-project it to $\{I_i\}_{i=1}^N$ and filter views that according to visibility (use the same visibility check function as in 4.2). The color observations for $\mathbf{v}$ can thus be represented by:

$$\mathbf{S}_{\mathbf{v}} = \{(\mathbf{c}_j, \mathbf{d}_j)\} = \{(\mathbf{c}_{\mathbf{v},j}, \mathrm{Norm}(\mathbf{o}_j - \mathbf{v}))\}_{j=1}^{N_{\text{vis}}}, \tag{5}$$

where N_{vis} is the number of views from where $\mathbf{v}$ can be seen and $\mathbf{o}_j$ is the corresponding camera center. These radiance sample points are used to fit a radiance map by computing the coefficients for the

SH expansion via least squares fitting:

$$\arg\min_{k_\ell^m} \sum_{j=1}^{N_{vis}} |\mathbf{c_v}(\mathbf{d}_j) - \mathbf{c}_j|^2, \tag{6}$$

where $k_\ell^m \in \mathbb{R}^3$ is a set of 3 coefficients for RGB components. Then, for each ray in $\tilde{\mathcal{R}}_\mathbf{v}$, color is determined by querying the SH functions Y_ℓ^m given its viewing direction $\mathbf{d}$. Using such an SH expansion to fit the radiance distribution can provide extrapolation for novel view direction.

To summarize, our method extends the training rays of NeRF considering scene geometry. For each surface vertice $\mathbf{v}$, we first construct $\tilde{\mathcal{R}}_\mathbf{v}$ by shooting random ray directions from $\mathbf{v}$ and filter invisible ones through visibility check. Since $\mathbf{v}$ can be observed at multiple input viewpoints, we model it as an SH which thus can be queried at any augmented ray direction going through $\mathbf{v}$.

4.4 Depth Warping

To best utilize the available information in the known view, we propose to propagate the depth information to other views through image warping. For pixel $p_i(x_i, y_i)$ in reference view I_{ref}, the corresponding pixel $p_j(x_j, y_j)$ in the jth unseen view I_{unseen} can be formulated as

$$p_j = K_{unseen} T \left(K_{\text{ref}}^{-1} Z_i p_i \right), \tag{7}$$

where Z_i is the available depth of reference view, T refers to the relationship between camera extrinsic matrices from I_{ref} to I_{unseen}, and K_{ref} and K_{unseen} refer to the camera intrinsic matrices. We further adopt the Painter's Algorithm when multiple points in the reference view are projected to the same point in the unseen view and select the point with the smallest depth as the warping result.

Through image warping, we can obtain a depth map of an unseen view, which can serve as a pseudo ground truth. Nevertheless, there is still an unavoidable gap between this pseudo ground truth and the real correspondence, since small misalignment in the predicted depth map can cause large errors when projected to other views. Moreover, it is quite common that the projected results contain some uncertain regions due to occlusion. To regularize the uncertain regions in the warped results, we utilize the self-supervised inverse depth smoothness loss, which uses the second-order gradients of the RGB pixel value to encourage the smoothness of the predicted depths:

$$\mathcal{L}_{smooth}(d_i) = e^{-\nabla^2 \mathcal{I}(\mathbf{x}_i)} \left(|\partial_{xx} d_i| + |\partial_{xy} d_i| + |\partial_{yy} d_i| \right), \tag{8}$$

where d_i is the depth map, $\nabla^2 \mathcal{I}(\mathbf{x}_i)$ refers to the Laplacian of pixel value at location x_i.

5 EXPERIMENTS

5.1 Novel Radiance Predicting from Spherical Harmonics

Firstly, we conduct an experiment to validate the effective method for generating radiance from unseen views. For predicting the novel radiance, we compare our method with a naive baseline: spherical linear interpolation, which interpolates the radiance of the unseen view from the nearest two seen views in the spherical coordinate system. Specifically, we implement the linear interpolation of radiance using the geodesic distance as the weight:

$$\hat{\mathbf{c}} = w\mathbf{c}_0 + (1 - w)\mathbf{c}_1, \tag{9}$$

$$w = \frac{d(\hat{\mathbf{v}}, \mathbf{v}_1)}{d(\mathbf{v}_1, \hat{\mathbf{v}}) + d(\hat{\mathbf{v}}, \mathbf{v}_2)}, \tag{10}$$

$$d(\mathbf{v}_1, \mathbf{v}_2) = \arctan \frac{|\mathbf{v}_1 \times \mathbf{v}_2|}{\mathbf{v}_1 \cdot \mathbf{v}_2}, \tag{11}$$

while $\hat{\mathbf{c}}, \hat{\mathbf{v}}$ are the radiance and view direction vector of novel view, $\{\mathbf{c}_i, \mathbf{v}_i | i \in 1, 2\}$ are these of the nearest two views, respectively. Intuitively, the spherical harmonics fitting method can provide extrapolation of radiance compared to the linear interpolation method while preserving the smoothing variation under the prior of harmonic function.

We generate a set of around 10,000 points with all of their visible colors from the KITTI dataset [15] for evaluating the two methods for radiance prediction. The radiance from different views of each point is divided into two training (known) and testing (unknown) views with ratios from 8 : 2 to 5 : 5, in order to evaluate the performance under the different number of novel views. We report the average normalized Mean Square Error (MSE) in the novel views in Table 1. The average MSE for SH fitting is less than that of interpolation, especially when the number of novel views exceeds the number of known views. A visualization case is shown in Figure 3.

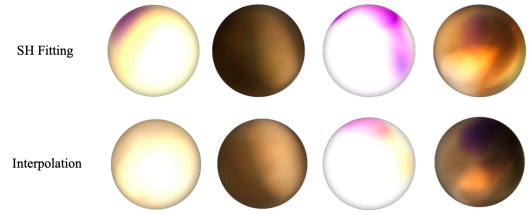

Figure 3: Visualization of radiance fitting. We project the radiance value of points distributed on the upper hemisphere into this circle to get a visualization of the fitted radiance distribution. The first row of images depicts the SH fitting results, while the second row showcases the outcomes of interpolation. It reveals that the SH fitting provides more informative radiance prediction results on the top line, while preserving the smoothness of distribution.

Table 1: MSE in the novel views between interpolation and SH fitting with different ratios between known rays and unknown rays.

Known/Unknown	8:2	7:3	6:4	5:5
Interpolation	0.0652	0.0744	0.0835	0.0951
SH Fitting	0.0602	0.0686	0.0779	0.0881

5.2 Implementation Details

Dataset In our experiments, we utilized three datasets known for their extensive capture of real-world driving scenarios: KITTI [15], Argoverse [5], and NuScenes [4]. These datasets are challenging for 3D reconstruction due to their object movement and lighting variations. From KITTI, we selected sequences with diverse driving conditions and reduced the data to simulate a 2.5 Hz capture

Table 2: Quantitative comparison with selected methods on the KITTI dataset. The best and the second best results are shown in bold and underlined forms, respectively.

	Dense				Sparse			
Methods	PSNR↑	SSIM↑	LPIPS↓	ABSREL↓	PSNR↑	SSIM↑	LPIPS↓	ABSREL↓
NeRF [28]	20.03	0.652	0.502	0.203	15.07	0.552	0.603	0.253
NSG [33]	20.56	0.664	0.482	0.192	15.54	0.564	0.582	0.244
pixelNeRF [53]	19.48	0.631	0.518	0.213	14.56	0.534	0.614	0.261
SUDS [44]	20.14	0.643	0.493	0.198	15.12	0.547	0.598	0.248
MARS [47]	20.43	0.658	0.478	0.187	15.38	0.558	0.573	0.237
Urban-NeRF [36]	20.72	0.678	0.457	0.184	15.76	0.572	0.553	0.226
MipNeRF-360 [3]	21.99	0.692	0.437	0.088	16.93	0.589	0.498	0.144
NeRF++ [56]	20.29	0.520	0.585	3.917	17.60	0.535	0.562	4.960
Instant-NGP [29]	20.51	0.630	0.460	**0.507**	15.44	0.499	0.536	0.793
Ours	**22.52**	**0.711**	**0.401**	0.087	**19.04**	**0.672**	**0.351**	**0.092**

Table 3: Evaluation and comparison of various methods on the NuScenes dataset. The best and the second best results are shown in bold and underlined forms, respectively.

	Dense				Sparse			
Methods	PSNR↑	SSIM↑	LPIPS↓	ABSREL↓	PSNR↑	SSIM↑	LPIPS↓	ABSREL↓
NeRF [28]	25.32	0.798	0.505	0.190	19.88	0.762	0.535	0.212
NSG [33]	26.10	0.810	0.498	0.185	20.34	0.770	0.528	0.208
pixelNeRF [53]	26.58	0.820	0.490	0.182	20.76	0.776	0.521	0.204
SUDS [44]	27.01	0.828	0.483	0.178	21.07	0.782	0.516	0.202
MARS [47]	27.45	0.835	0.475	0.173	21.50	0.790	0.510	0.198
Urban-NeRF [36]	27.92	0.843	0.461	0.169	20.09	0.802	0.504	0.195
MipNeRF-360 [3]	28.30	0.850	0.463	0.165	18.04	0.788	0.508	0.197
Instant-NGP [29]	27.80	0.840	0.472	0.170	16.42	0.780	0.512	0.243
Ours	**29.50**	**0.862**	**0.430**	**0.160**	**26.92**	**0.868**	**0.450**	**0.182**

frequency, using 25% of available frames. This subset is henceforth referred to as the 'sparse' dataset. In contrast, utilizing the entirety of the training set corresponds to a 'dense' data scenario. Similarly, for Argoverse, we halved the data to match its 5 Hz frequency. NuScenes provided additional complexity with its annotated 3D bounding boxes under various conditions. For each dataset, we reserved every tenth frame for testing and used the rest for training to assess our model's ability to handle sparse viewpoints effectively. The poses for image alignment were taken directly from the datasets' provided odometry and tracking data to maintain consistency with the actual scale of the scenes.

Implementation Details In general, we implement our ray augmentation strategy based on NeuS [46]. Previous work [30] has shown that the input encoding scheme is important for reconstructing an implicit representation. Thus, we compare and choose the frequency encoding [45] for the position input, and sphere harmonics function encoding [11] for the direction. We find that by replacing the frequency encoding with SH function encoding for direct input, the rendered color can converge faster.

We train our model using the Adam optimizer with an initial learning rate of $1e-4$ and a learning rate warm-up strategy. We choose a batch size of 2048 and train our model for 150k steps, and each scene is trained on one NVIDIA A100 GPU. To extract mesh for ray augmentation, we run marching cubes for a spatial resolution of 64^3 to get the vertices. The same algorithm is used for extracting mesh when we evaluate the reconstruction result.

Evaluation Metrics To validate the photorealism of our synthesized views against the ground truth, we employ widely accepted metrics from the field of novel view synthesis. Specifically, we measure the Peak Signal-to-Noise Ratio (PSNR), which reflects the reconstruction accuracy in terms of image pixel intensities. The Structural Similarity Index Measure (SSIM) assesses the perceived quality of the synthesized images, accounting for texture and structural integrity. Additionally, the Learned Perceptual Image Patch Similarity (LPIPS) metric evaluates the similarity between synthesized and ground truth images based on deep features, providing an estimate of perceptual likeness.

For the evaluation of depth reconstruction quality, we follow established precedents and include the Mean Absolute Relative Error (ABSREL) and the Root Mean Squared Error (RMSE). These depth accuracy metrics provide a quantitative measure of the disparity between the estimated depth maps and the ground truth, with ABSREL focusing on the relative difference and RMSE giving the Euclidean distance error.

5.3 Experiment Results

Quantitative Analysis

Table 4: Evaluation and comparison of various methods on the Argoverse dataset. The best and the second best results are shown in bold and underlined forms, respectively.

	Dense				Sparse			
Methods	PSNR↑	SSIM↑	LPIPS↓	ABSREL↓	PSNR↑	SSIM↑	LPIPS↓	ABSREL↓
NeRF [28]	26.54	0.812	0.491	0.185	21.44	0.785	0.521	0.205
NSG [33]	27.12	0.823	0.480	0.175	22.02	0.795	0.517	0.203
pixelNeRF [53]	27.64	0.831	0.477	0.175	22.63	0.805	0.502	0.196
SUDS [44]	27.88	0.835	0.462	0.165	23.01	0.814	0.495	0.190
MARS [47]	27.92	0.843	0.469	0.162	23.50	0.826	0.485	0.185
Urban-NeRF [36]	28.00	0.845	0.445	0.155	23.86	0.825	0.482	0.180
MipNeRF-360 [3]	29.35	0.855	0.446	0.120	25.81	0.829	0.468	0.139
Instant-NGP [29]	28.07	0.847	0.450	0.493	22.18	0.816	0.494	0.593
Ours	**30.25**	**0.865**	**0.430**	**0.110**	**29.50**	**0.874**	**0.450**	**0.130**

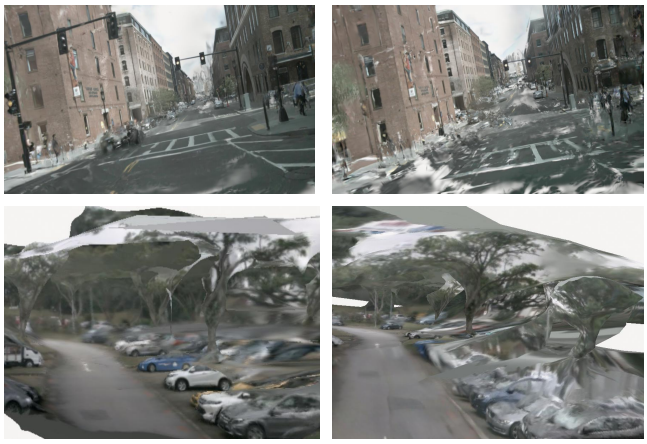

Figure 4: Visual comparison of scene reconstruction on the NuScenes dataset, contrasting HarmonicNeRF with MipNeRF-360 [3].

We conduct quantitative comparisons across the KITTI [15], NuScenes [4], and Argoverse [5] datasets to evaluate the performance of our method against several established baselines, including NeRF [28], NSG [33], pixelNeRF [53], SUDS [44], MARS [47], Urban-NeRF [36], MipNeRF-360 [3], and Instant-NGP [29].

In the dense scenario, our method consistently outperforms all baselines, achieving the highest PSNR and SSIM scores, while maintaining the lowest LPIPS and ABSREL scores across almost all three datasets. This indicates our approach's superior capability in synthesizing photorealistic views and reconstructing depth with high fidelity to the actual driving scenes.

The advantage of our method becomes even more pronounced in the sparse setting, where the limitations of existing techniques are more apparent due to reduced input data. Specifically, on the KITTI dataset, our method surpasses the second-best performing method, MipNeRF-360, by a significant margin in terms of PSNR (19.04 vs. 16.93) and SSIM (0.672 vs. 0.589), highlighting its effectiveness in dealing with sparse data. Similar trends are observed on the NuScenes and Argoverse datasets, where our method demonstrates exceptional performance, particularly in terms of PSNR and SSIM, further underscoring its robustness and adaptability to various driving scenarios.

These results not only underscore the efficacy of HarmonicNeRF in enhancing the quality of synthesized views and the accuracy of depth reconstructions under both data-rich and data-sparse conditions but also set a new benchmark for future research in 3D scene reconstruction from sparse views.

Qualitative Comparisons In addition to quantitative benchmarks, qualitative assessments on the KITTI dataset showcase the visual enhancements achieved with HarmonicNeRF. The comparison in Figure 5 reveals that, while Instant-NGP and MipNeRF-360 grapple with artifacts and blurring, particularly in motion-affected areas, HarmonicNeRF produces reconstructions with remarkable clarity and detail. Our method demonstrates superior texture fidelity and depth accuracy, capturing the nuances of urban driving scene complexity with greater photorealism.

On the NuScenes dataset, the superiority of HarmonicNeRF is further evidenced through visualizations presented in Figure 4. HarmonicNeRF excels in reconstructing densely populated urban areas, preserving distinct boundaries between objects, as shown on the left side of each comparison. In contrast, the right side displays results from MipNeRF-360, which, while competent, blends complex structures together—noticeably, trees meld with vehicles, and the finer architectural features are lost to blurring.

Ablation Study We dissect the components of HarmonicNeRF to understand their individual contributions, especially in sparse data contexts where the intricacies of each module are crucial. The ablation study results in Figure 6 highlight the impact of the key features under both dense and sparse conditions.

Without Spherical Harmonics: Replacing spherical harmonics with linear interpolation caused a noticeable performance drop. In sparse scenarios, this led to a substantial decrease in PSNR (e.g., by 2.8) and SSIM (e.g., by 0.03), validating the efficacy of spherical harmonics in handling limited data.

Without Visibility Checking: Without this component, our model was unable to effectively handle occlusions, with a significant increase in LPIPS (e.g., by 0.05) and a more pronounced decrease in

Figure 5: Qualitative comparison of 3D scene reconstructions from the KITTI dataset using different neural radiance field methods. The top row presents original images from diverse urban settings with varying levels of detail and complexity. HarmonicNeRF, which consistently provides the clearest and most accurate depictions, with crisp textures and fine details, effectively handling challenging lighting and occlusions, and showcasing a marked improvement in both the fidelity and photorealism of the reconstructed scenes.

SSIM in sparse data (e.g., by 0.04), confirming the crucial role of visibility checking in sparse view synthesis.

Alternative Ray Casting Methods: Substituting our surface-guided ray casting with random ray casting resulted in less accurate reconstructions, particularly under sparse conditions, where PSNR dropped by 3.0 and LPIPS increased by 0.04.

Without Depth Warping: Removing depth warping adversely affected depth estimation accuracy, especially in sparse setups, with ABSREL rising by 0.1, which points to the depth warping's substantial role in enhancing depth precision.

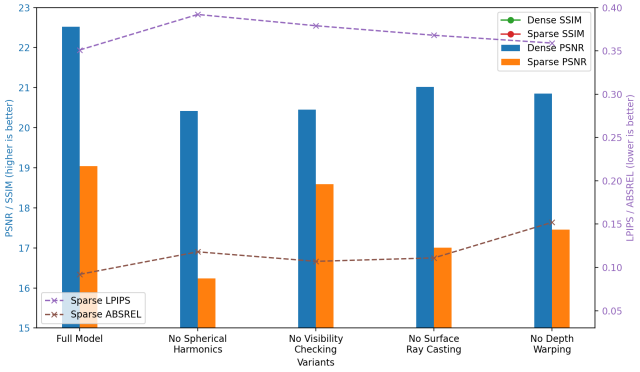

Figure 6: Ablation study results on the KITTI dataset, illustrating the impact of each component under dense and sparse conditions.

6 CONCLUSION

In this paper, we presented HarmonicNeRF addressing the significant challenge of sparse view reconstruction in the context of autonomous driving. Our approach innovatively enhances NeRF by integrating a geometry-guided ray augmentation strategy. This strategy not only employs a visibility check to filter out non-contributory rays using coarse geometry but also leverages spherical harmonics to model the natural distribution of radiance. This dual approach ensures physically plausible augmentations and superior surface reconstruction accuracy by effectively utilizing the limited observational data typical of unbounded outdoor scenes encountered in autonomous driving.

Our comprehensive experiments, spanning the KITTI, Argoverse, and NuScenes datasets, underscore HarmonicNeRF's ability to outperform existing methods significantly. By synthesizing novel depth views and reconstructing scenes with unprecedented precision, our method demonstrates its potential to set new standards for 3D scene reconstruction in autonomous driving applications.

However, limitations exist in our current framework. For instance, regions occluded in all observational views, such as the backside of objects, remain a challenge due to our visibility check's inability to augment such areas. Future endeavors could explore the integration of global scene priors or learning-based methods to infer these occluded regions.

REFERENCES

[1] Jonathan T Barron, Ben Mildenhall, Matthew Tancik, Peter Hedman, Ricardo Martin-Brualla, and Pratul P Srinivasan. 2021. Mip-nerf: A multiscale representation for anti-aliasing neural radiance fields. In *ICCV*.

[2] Jonathan T Barron, Ben Mildenhall, Matthew Tancik, Peter Hedman, Ricardo Martin-Brualla, and Pratul P Srinivasan. 2021. Mip-nerf: A multiscale representation for anti-aliasing neural radiance fields. In *Proceedings of the IEEE/CVF International Conference on Computer Vision*. 5855–5864.

[3] Jonathan T Barron, Ben Mildenhall, Dor Verbin, Pratul P Srinivasan, and Peter Hedman. 2022. Mip-nerf 360: Unbounded anti-aliased neural radiance fields. In *CVPR*.

[4] Holger Caesar, Varun Bankiti, Alex H Lang, Sourabh Vora, Venice Erin Liong, Qiang Xu, Anush Krishnan, Yu Pan, Giancarlo Baldan, and Oscar Beijbom. 2020. nuscenes: A multimodal dataset for autonomous driving. In *Proceedings of the IEEE/CVF conference on computer vision and pattern recognition*. 11621–11631.

[5] Ming-Fang Chang, John Lambert, Patsorn Sangkloy, Jagjeet Singh, Slawomir Bak, Andrew Hartnett, De Wang, Peter Carr, Simon Lucey, Deva Ramanan, et al. 2019. Argoverse: 3d tracking and forecasting with rich maps. In *Proceedings of the IEEE/CVF conference on computer vision and pattern recognition*. 8748–8757.

[6] Anpei Chen, Zexiang Xu, Fuqiang Zhao, Xiaoshuai Zhang, Fanbo Xiang, Jingyi Yu, and Hao Su. 2021. Mvsnerf: Fast generalizable radiance field reconstruction from multi-view stereo. In *Proceedings of the IEEE/CVF International Conference on Computer Vision*. 14124–14133.

[7] Rui Chen, Songfang Han, Jing Xu, and Hao Su. 2019. Point-based multi-view stereo network. In *Proceedings of the IEEE/CVF international conference on computer vision*. 1538–1547.

[8] Zhiqin Chen and Hao Zhang. 2019. Learning implicit fields for generative shape modeling. In *Proceedings of the IEEE/CVF Conference on Computer Vision and Pattern Recognition*. 5939–5948.

[9] Kangle Deng, Andrew Liu, Jun-Yan Zhu, and Deva Ramanan. 2022. Depth-supervised nerf: Fewer views and faster training for free. In *Proceedings of the IEEE/CVF Conference on Computer Vision and Pattern Recognition*. 12882–12891.

[10] Yilun Du, Yinan Zhang, Hong-Xing Yu, Joshua B Tenenbaum, and Jiajun Wu. 2021. Neural radiance flow for 4d view synthesis and video processing. In *2021 IEEE/CVF International Conference on Computer Vision (ICCV)*. IEEE Computer Society, 14304–14314.

[11] Sara Fridovich-Keil, Alex Yu, Matthew Tancik, Qinhong Chen, Benjamin Recht, and Angjoo Kanazawa. 2022. Plenoxels: Radiance Fields Without Neural Networks. In *Proceedings of the IEEE/CVF Conference on Computer Vision and Pattern Recognition*. 5501–5510.

[12] Yasutaka Furukawa, Carlos Hernández, et al. 2015. Multi-view stereo: A tutorial. *Foundations and Trends® in Computer Graphics and Vision* 9, 1-2 (2015), 1–148.

[13] Chen Gao, Ayush Saraf, Johannes Kopf, and Jia-Bin Huang. 2021. Dynamic view synthesis from dynamic monocular video. In *Proceedings of the IEEE/CVF International Conference on Computer Vision*. 5712–5721.

[14] Andreas Geiger, Philip Lenz, and Raquel Urtasun. 2012. Are we ready for autonomous driving? the kitti vision benchmark suite. In *2012 IEEE conference on computer vision and pattern recognition*. IEEE, 3354–3361.

[15] Andreas Geiger, Philip Lenz, and Raquel Urtasun. 2012. Are we ready for autonomous driving? the kitti vision benchmark suite. In *CVPR*.

[16] Benran Hu, Junkai Huang, Yichen Liu, Yu-Wing Tai, and Chi-Keung Tang. 2023. Nerf-rpn: A general framework for object detection in nerfs. In *Proceedings of the IEEE/CVF Conference on Computer Vision and Pattern Recognition*. 23528–23538.

[17] Ajay Jain, Matthew Tancik, and Pieter Abbeel. 2021. Putting nerf on a diet: Semantically consistent few-shot view synthesis. In *Proceedings of the IEEE/CVF International Conference on Computer Vision*. 5885–5894.

[18] Mohammad Mahdi Johari, Yann Lepoittevin, and François Fleuret. 2022. Geonerf: Generalizing nerf with geometry priors. In *Proceedings of the IEEE/CVF Conference on Computer Vision and Pattern Recognition*. 18365–18375.

[19] James T Kajiya and Brian P Von Herzen. 1984. Ray tracing volume densities. *ACM SIGGRAPH computer graphics* 18, 3 (1984), 165–174.

[20] Mijeong Kim, Seonguk Seo, and Bohyung Han. 2022. InfoNeRF: Ray Entropy Minimization for Few-Shot Neural Volume Rendering. In *Proceedings of the IEEE/CVF Conference on Computer Vision and Pattern Recognition*. 12912–12921.

[21] Zhuopeng Li, Lu Li, and Jianke Zhu. 2023. Read: Large-scale neural scene rendering for autonomous driving. In *Proceedings of the AAAI Conference on Artificial Intelligence*, Vol. 37. 1522–1529.

[22] Zhengqi Li, Simon Niklaus, Noah Snavely, and Oliver Wang. 2021. Neural scene flow fields for space-time view synthesis of dynamic scenes. In *Proceedings of the IEEE/CVF Conference on Computer Vision and Pattern Recognition*. 6498–6508.

[23] Yu-Lun Liu, Chen Gao, Andreas Meuleman, Hung-Yu Tseng, Ayush Saraf, Changil Kim, Yung-Yu Chuang, Johannes Kopf, and Jia-Bin Huang. 2023. Robust dynamic radiance fields. In *Proceedings of the IEEE/CVF Conference on Computer Vision and Pattern Recognition*. 13–23.

[24] William E Lorensen and Harvey E Cline. 1987. Marching cubes: A high resolution 3D surface construction algorithm. *ACM siggraph computer graphics* 21, 4 (1987), 163–169.

[25] Ricardo Martin-Brualla, Noha Radwan, Mehdi SM Sajjadi, Jonathan T Barron, Alexey Dosovitskiy, and Daniel Duckworth. 2021. Nerf in the wild: Neural radiance fields for unconstrained photo collections. In *CVPR*.

[26] Lars Mescheder, Michael Oechsle, Michael Niemeyer, Sebastian Nowozin, and Andreas Geiger. 2019. Occupancy networks: Learning 3d reconstruction in function space. In *Proceedings of the IEEE/CVF conference on computer vision and pattern recognition*. 4460–4470.

[27] Andreas Meuleman, Yu-Lun Liu, Chen Gao, Jia-Bin Huang, Changil Kim, Min H Kim, and Johannes Kopf. 2023. Progressively Optimized Local Radiance Fields for Robust View Synthesis. In *CVPR*.

[28] Ben Mildenhall, Pratul P Srinivasan, Matthew Tancik, Jonathan T Barron, Ravi Ramamoorthi, and Ren Ng. 2021. Nerf: Representing scenes as neural radiance fields for view synthesis. *Commun. ACM* 65, 1 (2021), 99–106.

[29] Thomas Müller, Alex Evans, Christoph Schied, and Alexander Keller. 2022. Instant Neural Graphics Primitives with a Multiresolution Hash Encoding. *ACM TOG* (2022).

[30] Thomas Müller, Alex Evans, Christoph Schied, and Alexander Keller. 2022. Instant Neural Graphics Primitives with a Multiresolution Hash Encoding. *ACM Trans. Graph.* 41, 4, Article 102 (July 2022), 15 pages. https://doi.org/10.1145/3528223.3530127

[31] Michael Niemeyer, Lars Mescheder, Michael Oechsle, and Andreas Geiger. 2020. Differentiable volumetric rendering: Learning implicit 3d representations without 3d supervision. In *Proceedings of the IEEE/CVF Conference on Computer Vision and Pattern Recognition*. 3504–3515.

[32] Michael Oechsle, Songyou Peng, and Andreas Geiger. 2021. Unisurf: Unifying neural implicit surfaces and radiance fields for multi-view reconstruction. In *Proceedings of the IEEE/CVF International Conference on Computer Vision*. 5589–5599.

[33] Julian Ost, Fahim Mannan, Nils Thuerey, Julian Knodt, and Felix Heide. 2021. Neural scene graphs for dynamic scenes. In *Proceedings of the IEEE/CVF Conference on Computer Vision and Pattern Recognition*. 2856–2865.

[34] Jeong Joon Park, Peter Florence, Julian Straub, Richard Newcombe, and Steven Lovegrove. 2019. Deepsdf: Learning continuous signed distance functions for shape representation. In *Proceedings of the IEEE/CVF conference on computer vision and pattern recognition*. 165–174.

[35] Albert Pumarola, Enric Corona, Gerard Pons-Moll, and Francesc Moreno-Noguer. 2021. D-nerf: Neural radiance fields for dynamic scenes. In *Proceedings of the IEEE/CVF Conference on Computer Vision and Pattern Recognition*. 10318–10327.

[36] Konstantinos Rematas, Andrew Liu, Pratul P Srinivasan, Jonathan T Barron, Andrea Tagliasacchi, Thomas Funkhouser, and Vittorio Ferrari. 2022. Urban radiance fields. In *CVPR*.

[37] Vincent Sitzmann, Justus Thies, Felix Heide, Matthias Nießner, Gordon Wetzstein, and Michael Zollhofer. 2019. Deepvoxels: Learning persistent 3d feature embeddings. In *Proceedings of the IEEE/CVF Conference on Computer Vision and Pattern Recognition*. 2437–2446.

[38] Vincent Sitzmann, Michael Zollhöfer, and Gordon Wetzstein. 2019. Scene representation networks: Continuous 3d-structure-aware neural scene representations. *Advances in Neural Information Processing Systems* 32 (2019).

[39] Jiaming Sun, Xi Chen, Qianqian Wang, Zhengqi Li, Hadar Averbuch-Elor, Xiaowei Zhou, and Noah Snavely. 2022. Neural 3D Reconstruction in the Wild. In *ACM SIGGRAPH 2022 Conference Proceedings*. 1–9.

[40] Matthew Tancik, Vincent Casser, Xinchen Yan, Sabeek Pradhan, Ben Mildenhall, Pratul P Srinivasan, Jonathan T Barron, and Henrik Kretzschmar. 2022. Block-nerf: Scalable large scene neural view synthesis. In *CVPR*.

[41] Edgar Tretschk, Ayush Tewari, Vladislav Golyanik, Michael Zollhöfer, Christoph Lassner, and Christian Theobalt. 2021. Non-rigid neural radiance fields: Reconstruction and novel view synthesis of a dynamic scene from monocular video. In *Proceedings of the IEEE/CVF International Conference on Computer Vision*. 12959–12970.

[42] Alex Trevithick and Bo Yang. 2021. Grf: Learning a general radiance field for 3d representation and rendering. In *ICCV*.

[43] Haithem Turki, Deva Ramanan, and Mahadev Satyanarayanan. 2022. Mega-NeRF: Scalable Construction of Large-Scale NeRFs for Virtual Fly-Throughs. In *CVPR*.

[44] Haithem Turki, Jason Y Zhang, Francesco Ferroni, and Deva Ramanan. 2023. Suds: Scalable urban dynamic scenes. In *Proceedings of the IEEE/CVF Conference on Computer Vision and Pattern Recognition*. 12375–12385.

[45] Chen Wang, Xian Wu, Yuan-Chen Guo, Song-Hai Zhang, Yu-Wing Tai, and Shi-Min Hu. 2022. NeRF-SR: High Quality Neural Radiance Fields using Super-sampling. In *Proceedings of the 30th ACM International Conference on Multimedia*. 6445–6454.

[46] Peng Wang, Lingjie Liu, Yuan Liu, Christian Theobalt, Taku Komura, and Wenping Wang. 2021. Neus: Learning neural implicit surfaces by volume rendering for multi-view reconstruction. *arXiv preprint arXiv:2106.10689* (2021).

[47] Zirui Wu, Tianyu Liu, Liyi Luo, Zhide Zhong, Jianteng Chen, Hongmin Xiao, Chao Hou, Haozhe Lou, Yuantao Chen, Runyi Yang, et al. 2023. Mars: An instance-aware, modular and realistic simulator for autonomous driving. In *CAAI International Conference on Artificial Intelligence*. Springer, 3–15.

[48] Ziyang Xie, Junge Zhang, Wenye Li, Feihu Zhang, and Li Zhang. 2023. S-NeRF: Neural Radiance Fields for Street Views. *arXiv preprint arXiv:2303.00749* (2023).

[49] Qiangeng Xu, Zexiang Xu, Julien Philip, Sai Bi, Zhixin Shu, Kalyan Sunkavalli, and Ulrich Neumann. 2022. Point-nerf: Point-based neural radiance fields. In *CVPR*.

[50] Yao Yao, Zixin Luo, Shiwei Li, Tian Fang, and Long Quan. 2018. Mvsnet: Depth inference for unstructured multi-view stereo. In *Proceedings of the European conference on computer vision (ECCV)*. 767–783.

[51] Lior Yariv, Jiatao Gu, Yoni Kasten, and Yaron Lipman. 2021. Volume rendering of neural implicit surfaces. *Advances in Neural Information Processing Systems* 34 (2021), 4805–4815.

[52] Lior Yariv, Yoni Kasten, Dror Moran, Meirav Galun, Matan Atzmon, Basri Ronen, and Yaron Lipman. 2020. Multiview neural surface reconstruction by disentangling geometry and appearance. *Advances in Neural Information Processing Systems* 33 (2020), 2492–2502.

[53] Alex Yu, Vickie Ye, Matthew Tancik, and Angjoo Kanazawa. 2021. pixelnerf: Neural radiance fields from one or few images. In *Proceedings of the IEEE/CVF Conference on Computer Vision and Pattern Recognition*. 4578–4587.

[54] Jingyang Zhang, Yao Yao, and Long Quan. 2021. Learning signed distance field for multi-view surface reconstruction. In *Proceedings of the IEEE/CVF International Conference on Computer Vision*. 6525–6534.

[55] Jian Zhang, Yuanqing Zhang, Huan Fu, Xiaowei Zhou, Bowen Cai, Jinchi Huang, Rongfei Jia, Binqiang Zhao, and Xing Tang. 2022. Ray Priors through Reprojection: Improving Neural Radiance Fields for Novel View Extrapolation. In *Proceedings of the IEEE/CVF Conference on Computer Vision and Pattern Recognition*. 18376–18386.

[56] Kai Zhang, Gernot Riegler, Noah Snavely, and Vladlen Koltun. 2020. Nerf++: Analyzing and improving neural radiance fields. *arXiv preprint arXiv:2010.07492* (2020).